



# Flows around Averaged Solar Active Regions

D. C. Braun

NorthWest Research Associates, 3380 Mitchell Lane, Boulder, CO 80301, USA; [dbraun@nwra.com](mailto:dbraun@nwra.com)  
Received 2019 January 7; revised 2019 February 3; accepted 2019 February 4; published 2019 March 7

## Abstract

We explore the general properties of near-surface flows around solar active regions. Helioseismic holography is applied to HMI Dopplergrams yielding nearly 5000 flow measurements of 336 unique active regions observed by the *Solar Dynamics Observatory* between 2010 and 2014. Ensemble averages of the flows, over subsets of regions sorted on the basis of magnetic flux, are performed. These averages show that converging flows, with speeds of about  $10 \text{ m s}^{-1}$  and extending up to  $10^\circ$  from the active-region centers, are prevalent and have similar properties for all regions with magnetic flux above  $10^{21} \text{ Mx}$ . Retrograde flows are also detected, with amplitudes around  $10 \text{ m s}^{-1}$ , which predominantly, but not exclusively, flank the polar side of the active regions. We estimate the expected contribution of these active-region flows to longitudinal averages of zonal and meridional flows and demonstrate the plausibility that they are responsible for at least some component of the time-varying global-scale flows. The reliability of our flow determination is tested using publicly available MHD simulations of both quiet-Sun convection and of a sunspot. While validating the overall methodology in general, the sunspot simulation demonstrates the presence of artifacts that may compromise quantitative flow inferences from some helioseismic measurements.

*Key words:* Sun: activity – Sun: helioseismology – Sun: magnetic fields – sunspots

## 1. Introduction

The detection of flows with amplitudes of order  $10 \text{ m s}^{-1}$  or more and converging toward active regions (hereafter ARs) was an early discovery in local helioseismology (Gizon et al. 2001; Haber et al. 2004; Zhao & Kosovichev 2004). However, their general characteristics, including their detailed variation with magnetic properties of the associated magnetic regions, remain largely uncharted. These flows appear to provide a link between convection and magnetism, two critical processes governing the solar convection zone. Possibly lasting (at least) as long as the magnetic regions themselves, the flows are suspected of affecting larger circulation patterns, particularly the meridional and zonal flow components of global circulation. For example, converging flows in AR latitudes appear to modulate and reduce the amplitude of the meridional flow pattern (Chou & Dai 2001; Gizon 2003; Zhao & Kosovichev 2004). The meridional flow is involved critically in the process that leads to polar field polarity reversals (Wang et al. 2002) and the ability to predict properties of subsequent solar cycles (e.g., as reviewed by Jiang et al. 2014). The modulation associated with active latitudes, and which may include AR-related inflows, is believed to provide critical nonlinear feedback, preventing eventual decay or growth of subsequent solar cycles (e.g., Jiang et al. 2010; Cameron & Schüssler 2012; Martin-Belda & Cameron 2017). The role of this modulation has been explored as a contributor to the recent extended solar minimum and weak cycle 24 (Upton & Hathaway 2014).

Early measurements were made of the subsurface flows beneath individual ARs (Haber et al. 2004; Zhao & Kosovichev 2004), which are described as a toroidal-like circulation with converging flows extending down to depths of about 10 Mm and diverging flows below this depth. As reviewed by Gizon et al. (2010) this scenario is far from established and relevant systematic surveys have been sparse. Some general properties of the flows and their relation to other AR properties have been studied (Komm et al. 2007, 2011; Komm & Gosain 2015), albeit with helioseismic methods with relatively low spatial resolution

(i.e., having spatial scales on the order of  $15^\circ$ , which is comparable to the AR sizes). The ring-diagram based survey performed by Hindman et al. (2009) focused on the near-surface ( $<2 \text{ Mm}$  deep) flow properties, including inflow and circulation speeds, of  $\sim 100$  ARs at somewhat higher spatial resolution ( $\sim 2^\circ$ ).

Studies of near-surface flows using helioseismic methods with greater spatial resolution are hampered by the strong flows associated with supergranulation. Supergranules with peak flows  $\sim 300 \text{ m s}^{-1}$  (Rincon & Rieutord 2018), and root-mean-squared (rms) fluctuations  $\sim 100 \text{ m s}^{-1}$ , effectively act as noise and dominate the weaker flows associated with ARs. Ensemble averaging, consisting of identifying and averaging coaligned flow measurements of features with (expected) similar properties provides one method for increasing the signal-to-noise ratio. Löptien et al. (2017), using a local-correlation tracking method applied to the granulation pattern, carried out such averaging over more than 200 ARs. In this work, we carry out a high spatial resolution ( $\sim 1^\circ$ ) survey of ARs flows, using helioseismic holography (hereafter HH) applied to Dopplergrams obtained from the Helioseismic and Magnetic Imager (HMI). Our intent is to measure and compare ensemble-averaged AR flows across a wide range of magnetic flux. To accomplish this, we use both existing (Braun 2016) flow measurements of 252 large (NOAA numbered) ARs, as well as additional measurements of flows around regions with magnetic fluxes as low as  $10^{21} \text{ Mx}$ . Our survey is discussed in Section 2, which includes a description of AR identification (Section 2.1), and the magnetic properties of the complete sample (Section 2.2). The “calibrated-HH” method, employed to infer the near-surface flows, is described in Section 2.3. Results are presented in Section 3, followed by a discussion in Section 4.

## 2. Survey

The starting point of our flow survey is the HH analysis by Braun (2016). This prior survey, carried out to probe the

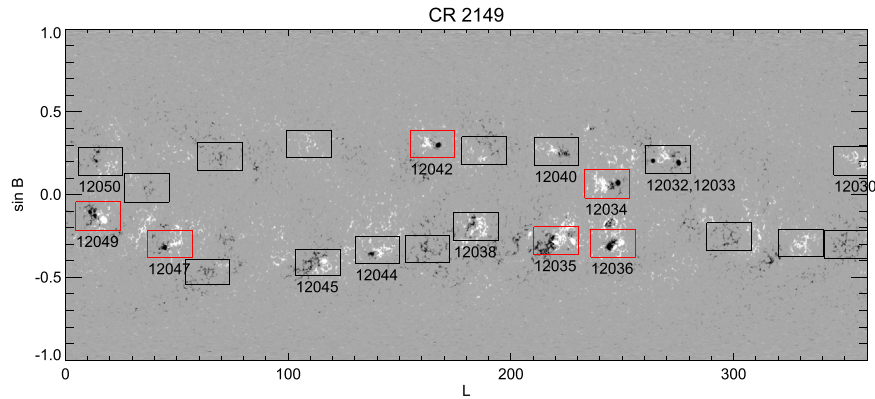


**Figure 1.** SDO/HMI synoptic magnetogram for Carrington rotation 2149, showing some active regions selected for this survey. Red boxes enclose large sunspot groups that were previously identified and analyzed (Braun 2016) on the basis of NOAA published sunspot areas. Black boxes indicate (mostly weaker) regions that are included in this survey using the identification method described in the text. Some of these regions are labeled by one (or more) NOAA sunspot numbers; others have no NOAA designation.

relationship between flows and solar flares, produced approximately 4000 sets of near-surface flow maps of 252 unique NOAA numbered sunspot regions present between 2010 May and 2014 December. The use of the largest sunspot groups (as ranked by sunspot areas) was appropriate for studies of solar flares, but for the present work we have extended the AR sample to include weaker regions. The method used to identify these additional regions is described below.

### 2.1. Selection

To achieve a representative sample of ARs for a given solar rotation we start with HMI synoptic magnetograms. Taking the absolute value of the magnetic flux density, we applied spatial smoothing with a two-dimensional Gaussian function with a full width at half maximum (FWHM) of  $10^\circ$ . We located all of the peaks in this smoothed map, where a peak is defined to have a pixel value greater than the eight neighboring pixels. Sorting the peaks from highest to lowest magnetic flux density, we discard those that are situated within  $20^\circ$  of any larger peak. The total unsigned flux of each candidate AR (contained within a  $20^\circ \times 10^\circ$  bounding box) were assessed from the synoptic magnetogram, and only regions with a total flux greater than  $10^{21}$  Mx (the lower limit of this survey) were retained. While the method is not intended to identify all possible magnetic regions, it does select ones that are more spatially separated from each other. This allows the flows associated with those regions to be more readily isolated.

We employ this procedure to six Carrington rotations, spaced 10 rotations apart, and spanning the time range of the Braun (2016) survey (specifically, these included Carrington rotation numbers CR 2099, 2109, 2119, 2129, 2139, and 2149). An example of the regions identified for CR 2149 (the most active rotation) is given by Figure 1. A total of 104 ARs are identified in this manner during the six rotations, of which 20 are part of the Braun (2016) survey. Our complete sample thus contains 336 unique ARs: 252 from the original flare survey plus 84 new regions.

### 2.2. Magnetic Properties

Datacubes of Dopplergrams and magnetograms, centered on the AR locations determined using the procedure described above, are constructed identically to those employed by Braun (2016). Specifically, full-disk HMI magnetograms and

Dopplergrams are remapped to Postel coordinates ( $x_p, y_p$ ) with a tangent point centered on the AR location, tracked with a fixed Carrington rate, and spanning  $30^\circ$  by  $30^\circ$  with a pixel spacing of  $0.0573$ . The choice of the Carrington rate, historically derived from observations of sunspots and defined as one rotation per 27.2753 days as viewed from Earth, is motivated by the desire to minimize spatial drifting of ARs in the Doppler and magnetogram time series. Further analysis to remove contributions from large-scale flows, including departures from the Carrington rotation rate, is described in Section 3.1. We use full-disk Dopplergrams with the full cadence of 45 seconds for the HH analysis of flows discussed in Section 2.3.

The magnetic properties of each AR are studied from remapped full-disk magnetograms sampled every 68 minutes. The passage of each AR across the disk is divided into 16 nonoverlapping intervals each spanning 13.6 hr. To ensure the quality of the helioseismic analysis, intervals for which the AR position was farther than  $60^\circ$  from disk center, or for which gaps in the HMI Dopplergram data exceeded 30% of the 13.6 hr period are excluded from further study.

For each AR, the Postel-remapped magnetograms are averaged over each of the 13.6 hr intervals. For the purpose of coalignment necessary for ensemble averaging, positions defining the center of mass (centroid) of the unsigned magnetic flux density, relative to the Postel-projection center, are obtained. During this step, the net unsigned flux (corrected for the cosine of the heliocentric angle) is also integrated and recorded. To reduce the effect of magnetogram noise, only pixels with flux density greater than 50 G present in a  $20^\circ \times 10^\circ$  bounding box are retained in the centroid and flux determinations. The statistics of these position offsets were examined, and a rejection of time intervals for which the offset (in either the  $x_p$  or  $y_p$  coordinate of the Postel frame) exceeded the mean by plus-or-minus three standard deviations was carried out. Values of the standard deviations are  $1.2$  and  $0.6$  in the  $x_p$  and  $y_p$  directions, respectively.

After the analysis and data rejection described above, we are left with 4925 measurement sets that exceed  $10^{21}$  Mx flux. A histogram of the fluxes is shown in Figure 2. The distribution is divided into five flux groups as separated by the vertical lines in the figure. Some properties of the groups are listed in Table 1, including the defining flux range, the median flux ( $\Phi_{\text{med}}$ ) for each group, and the number of measurements within each

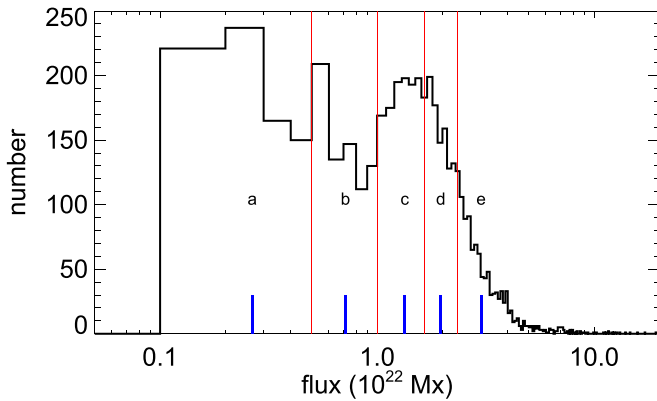


**Figure 2.** Histogram of the magnetic flux determined over 4925 time intervals of magnetograms of the 336 active regions studied in this work. Red lines delineate the flux groups selected for study, with the blue markers indicating the median flux of each group sample.

group. The magnetic flux in most ARs change over the 9 days they are tracked, resulting in most regions being included in more than a single flux group. Magnetograms of ARs, randomly selected from each group, are shown in the top row of Figure 3. Coaligned averages over each group of the signed line-of-sight magnetic flux density are shown in the bottom row of Figure 3. For the averaging, we adapt a coordinate system  $(x, y)$  with an origin at the center-of-mass,  $x$  increasing in the westward (prograde) direction, and  $y$  increasing toward the pole of the hemisphere in which the AR resides. Thus, ARs in the southern hemisphere are spatially flipped around the  $x_p$  axis. In accordance with Hale’s polarity law, regions in the southern hemisphere also have their polarity switched. The group averages clearly show the two polarities, tilted by Joy’s law, and having an asymmetry in peak flux density between polarities.

### 2.3. Calibrated-HH Flows

We use HH in the so-called lateral-vantage geometry (e.g., Lindsey & Braun 2004) and with a focus depth of 3 Mm below the photosphere. This method is analogous to deep-focus methods in time–distance helioseismology and common-depth-point reflection terrestrial seismology. The result is the determination of travel-time differences of waves propagating between opposite quadrants of an annular pupil. As was carried out in our prior analysis (Braun 2016), we use a simple numerical calibration to directly convert the travel-time differences to components of the flow. This calibration is based on assumptions that include: (1) the sensitivity function, which relates the three-dimensional flow properties to the resulting travel-time difference, is compact in volume relative to the spatial scale of the inferred flows, and (2) the horizontal flow components (rather than vertical ones) produce the principle contribution to the time differences. Similar calibration procedures have been extensively used, particularly for the study of shallow flows, with both  $f$ -modes (Gizon et al. 2001, 2003) and high-degree  $p$ -modes (Braun et al. 2004; Braun & Wan 2011; Birch et al. 2016; Braun 2016). The calibration constant, relating the west-minus-east (WE) and north-minus-south (NS) travel-time difference into westward and northward vector components is deduced by the application of two different tracking rates to a time-series of Dopplergrams of a region on the Sun. The weighting in depth

**Table 1**  
Properties of Magnetic Flux Groups

Group	$\Phi$ Range ( $10^{22}$ Mx)	$\Phi_{\text{med}}$ ( $10^{22}$ Mx)	Number
a	0.1–0.5	0.27	773
b	0.5–1.0	0.71	733
c	1.0–1.67	1.34	1234
d	1.67–2.35	1.97	1088
e	>2.35	3.01	1097

of the subsurface horizontal flows that contribute to the measurements can be (roughly) characterized by the horizontal integral of the sensitivity function. For the measurements used here, this weighting is plotted in Figure 4. The sensitivity function shown is derived using the Born approximation and is described by DeGrave et al. (2018).

Comparisons between results obtained from calibrated-HH methods and nonhelioseismic procedures (e.g., local-correlation tracking) have been successfully performed (e.g., Birch et al. 2016). The construction of realistic numerical simulations of wave propagation within solar-like model interiors has allowed the direct testing of helioseismic methods (e.g., Braun et al. 2007; Zhao et al. 2007; Braun et al. 2012; DeGrave et al. 2014a, 2018) In Appendix A, we use publicly available MHD simulations, of both solar convection and realistic sunspots, to validate the calibrated flows used in this work.

## 3. Results

Ensemble averages of the calibrated-HH flow components for each flux group are made, after coaligning each flow map. This alignment uses the same center-of-mass positions determined from the magnetograms (Section 2.2). The remapping to the center-of-mass distances  $(x, y)$  is performed on each flow component using bicubic interpolation.

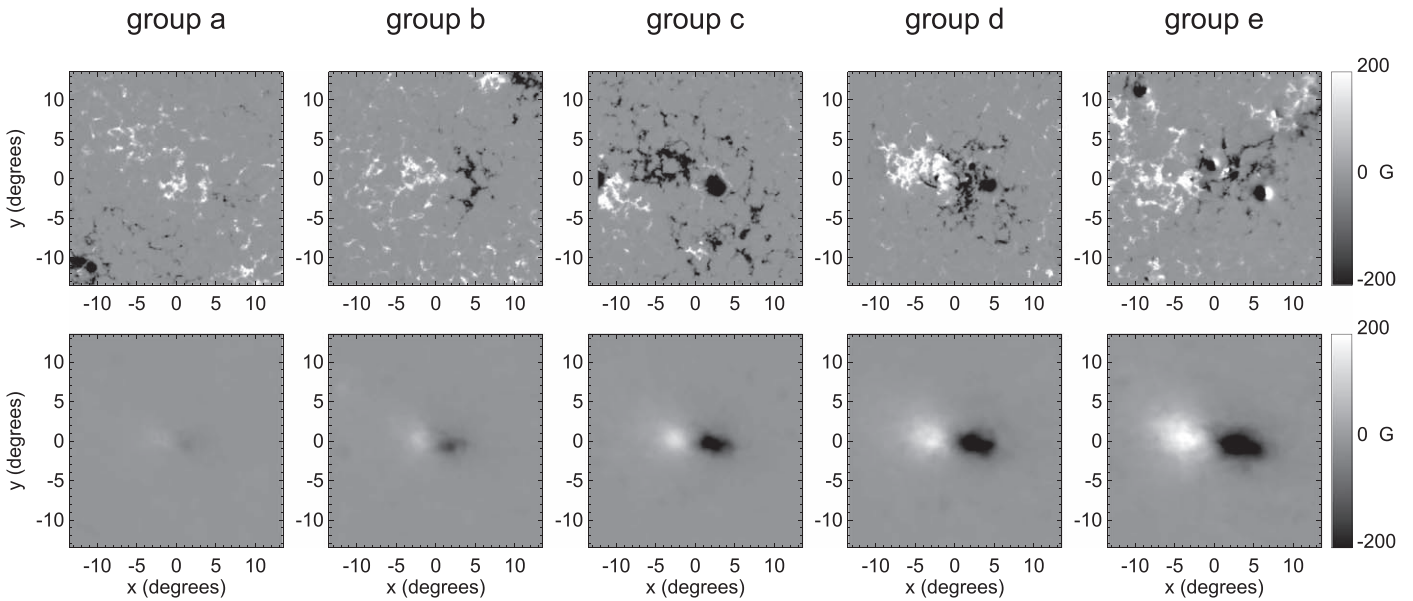
### 3.1. Large-scale Detrending

Large-scale background flows, including differential rotation and meridional flow, are removed from the ensemble-averaged flow components by fitting a quadratic polynomial in  $y$  to the average of two vertical “quiet-Sun” strips of the component maps situated near the east and west edges of the averaged frame (Figure 5). The assumption that the background flows vary only with  $y$  is based on the near alignment of this axis with the meridional direction in each of the Postel projections contributing to the ensemble averages. We note that this detrending removes any signal due to the departure of the real solar (latitude-dependent) rotation from the tracked Carrington rate. Implications of this detrending for our results are further discussed in Section 4.

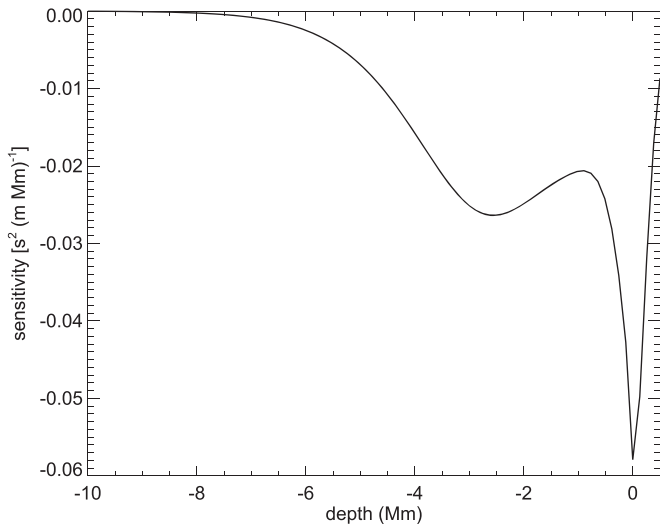
### 3.2. Ensemble Averages

Figure 6 shows the ensemble-averaged flows for each flux group after detrending is applied. For the purpose of clarity, strong diverging flows due to sunspots have been suppressed in Figure 6. However, a version of this figure showing the complete flow fields (Figure 12) is presented in Appendix B.

Whereas comparable flow maps of individual ARs show rms fluctuations of  $\sim 100 \text{ m s}^{-1}$  due to supergranulation, we estimate a  $\sim 5 \text{ m s}^{-1}$  error in each flow component of the averages shown in Figure 6. This value is consistently derived



**Figure 3.** Magnetic appearance of active regions divided into five groups of increasing total magnetic flux. The top row shows 13.6 hr averages of magnetograms for a randomly selected AR sample in each group while the column below that shows the ensemble average of the signed magnetic flux density after coaligning the magnetograms to their center of mass (as determined from the unsigned flux density). The coordinate system is defined as the distance from the center-of-mass toward the west ( $x$ ) and toward the pole ( $y$ ) of the hemisphere in which the AR resides.



**Figure 4.** Depth dependence of the horizontally integrated sensitivity kernel, relating the contribution of a horizontal flow component to the lateral-vantage travel-time difference as measured across opposite quadrants and for a nominal focus depth of 3 Mm. This function roughly describes the relative weight in depth of the true flows contributing to our calibrated flow maps. There is a peak in the sensitivity at the photosphere and a weaker peak around the nominal focus depth. Adapted from Figure 13 of DeGrave et al. (2018).

from measurements of both: (1) the rms pixel-to-pixel fluctuations within selected regions of the maps and (2) the rms fluctuations, at a given pixel, among subsamples of ARs in each flux group. In Section 3.3 we show quantitative comparisons of some aspects of these flow maps, but some general findings from these maps are notable. In particular, all flux groups show flows converging from nearby quiet-Sun regions extending between  $2^\circ$  and  $10^\circ$  from both the polar and equatorial sides of the AR.

Despite a wide variation of magnetic flux across the different groups, both the amplitude and spatial extension of the inflows

appear similar for all groups. Another distinct trend is that, for most flux groups, the bulk of the flows in both of these flanking regions have a net eastward (retrograde) component. Both of these findings are discussed below.

### 3.3. Flow Variations with AR Flux

To compare the flows around ARs among different flux groups, we average the flow components over a modest range in longitude. Longitudinal averages are useful to examine the potential contribution of these AR-related flows to global meridional or zonal (e.g., torsional oscillation) patterns and is discussed in Section 3.4. Motivated by apparent asymmetries between the two polarity regions, we average over  $6^\circ$  longitude ranges isolating either the leading and trailing regimes as defined by the vertical white lines in Figure 6.

Further discussion of our findings separate the inferred flows into two regimes: those confined to within  $3^\circ$  of the AR center latitude and those extending beyond this distance. The reason for this distinction is the greater uncertainty in inferences in the former group, based on our tests of HH using MHD simulations of both sunspots and quiet-Sun convection (Appendix A). Those tests confirm that strong deviations between inferred and true flows exist within the penumbral boundary of simulated spots. In addition, while the moat flows (extending about 30 Mm from the simulated sunspot) are qualitatively reproduced, the amplitudes appear to be systematically underestimated (Figure 10). Appropriate caveats should therefore be applied to the results relevant to the flows near or within the ARs themselves, which we discuss first.

Close to the AR centers (i.e., within the vertical dashed lines in Figure 7) outflows are present in the meridional flow component  $v_y$  from both polarities of most magnetic regions. Only the weakest ARs (group (a)) do not show a central divergence from the leading polarity, while all but groups (a) and (b) show diverging flows from the trailing polarity. The outflows increase in magnitude with higher flux, which is likely an indication of an increasing number of larger sunspots.

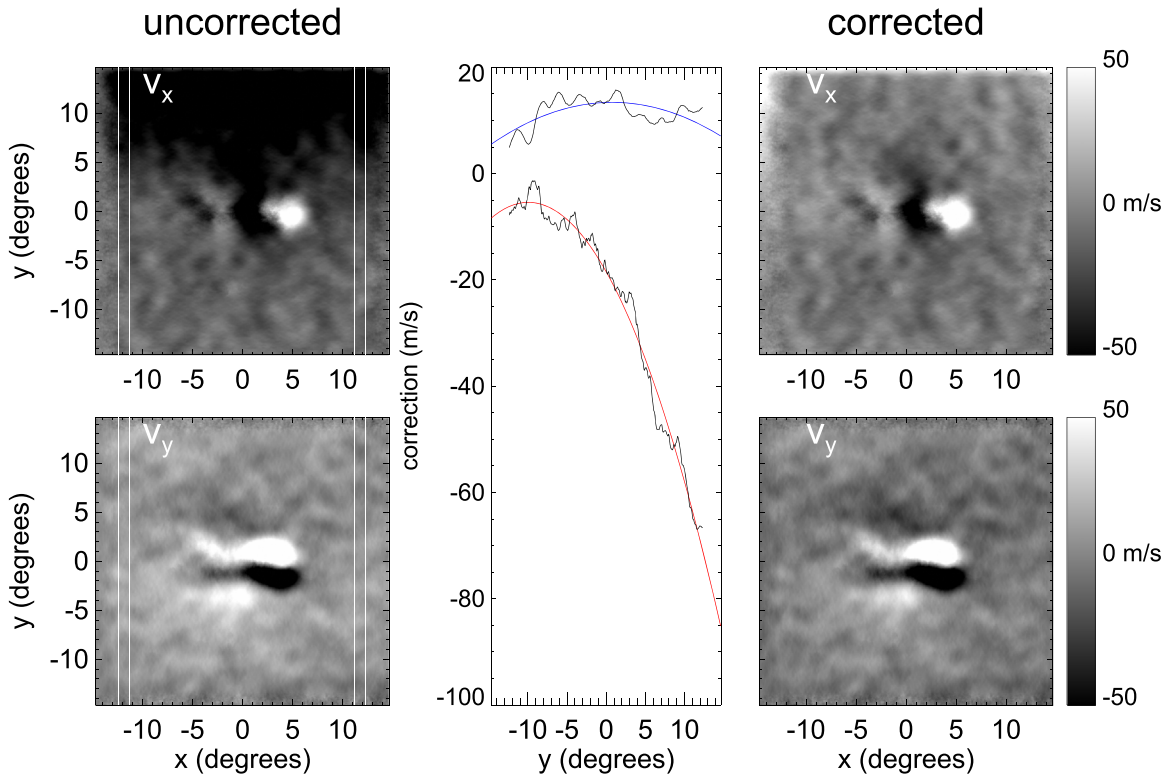


**Figure 5.** Demonstration of the removal of large-scale background flows from the flow components for group (d) (results for other groups are similar). The left two panels show the raw  $v_x$  (top) and  $v_y$  (bottom) components, with “quiet” bands outlined by vertical white lines on the edges of the frame. The values in the quiet regions are averaged horizontally across the two bands and plotted against  $y$  in the center line plot. Polynomial fits to these data are overlaid for the  $v_x$  (red) component and  $v_y$  (blue) component, respectively. The flow component maps on the right show the residuals after these polynomials are subtracted from each column of the uncorrected maps. The gray scales on the right showing speed in  $\text{m s}^{-1}$  apply to both the uncorrected and corrected maps.

The zonal component  $v_x$  within magnetic regions also shows variations with flux. Within the leading polarity, most ARs (with the exception of group (a)) show prograde flows. This is consistent with prior inferences of prograde motion in ARs (e.g., Braun et al. 2004; Zhao & Kosovichev 2004). In the trailing polarity, the stronger regions (groups (c) through (e)) exhibit retrograde motions while the weaker groups (a) and (b) show prograde flows. A simple picture at least roughly consistent with these trends is that, with respect to the polarity boundary, one observes diverging flows from stronger regions but convergence in weaker regions.

Turning to the flows extending beyond  $3^\circ$  of the AR center latitude (i.e., outside of the vertical dashed lines in Figure 7), the predominant inference from the meridional components is the presence of inflows extending up to about  $10^\circ$  from the AR centers. These inflows sometimes have magnitudes as strong as  $20$  or  $30 \text{ m s}^{-1}$  close to the AR, but are typically about  $10 \text{ m s}^{-1}$  farther away from the ARs. From the meridional components alone it is apparent that the inflows are stronger into the trailing polarity than the leading polarity. The converging flows into the trailing polarity appear to increase in amplitude (with reasonable significance above formal errors) with increasing flux, but are invariant (within errors) with respect to flux into the leading polarity. The inflows are mostly symmetric about the central latitude.

Eastward (retrograde) flows are present in most regions, also with  $10 \text{ m s}^{-1}$  amplitudes and extending to  $10^\circ$  from the AR centers. Retrograde flows flank both the leading and trailing polarities, suggesting that they are a feature distinct from, and not simply caused by, the convergence toward the trailing

polarity. In general, the retrograde flows occur predominantly on the polar side. This asymmetry is particularly notable above and below the trailing polarity in all groups. In the leading polarity, the retrograde flows increase with flux on the equatorial side, such that the strongest regions show similar amplitudes on both sides.

A reasonable question is how systematic errors due to strong magnetic fields (as revealed, for example, in Appendix A) may influence these inferences given the averaging over many ARs with different morphologies. For example, individual ARs may include sunspots or other strong field regions that are significantly displaced by many degrees from the center of the averaged AR, and thus potentially compromise measurements of flows at these corresponding locations. Appendix C shows the results of a direct test of this issue, whereby ensemble averages are performed with spatial masks applied to exclude flows within strong magnetic fields. These tests indicate a high robustness of flow inferences  $3^\circ$  away from the central AR latitude.

### 3.4. Contribution to Global Meridional and Zonal Flows

Flows surrounding ARs may contribute, even inadvertently, to assessments of the longitudinal averages of global flow patterns including the differential rotation and meridional circulation. Quantifying this contribution is particularly important in interpreting or modeling the solar-cycle variations of these flows and, in turn, making long-term predictions about the Sun. Measurements of the 11 yr variability in both the meridional circulation and the differential rotation (with the latter variability dominated by the “torsional oscillation”)

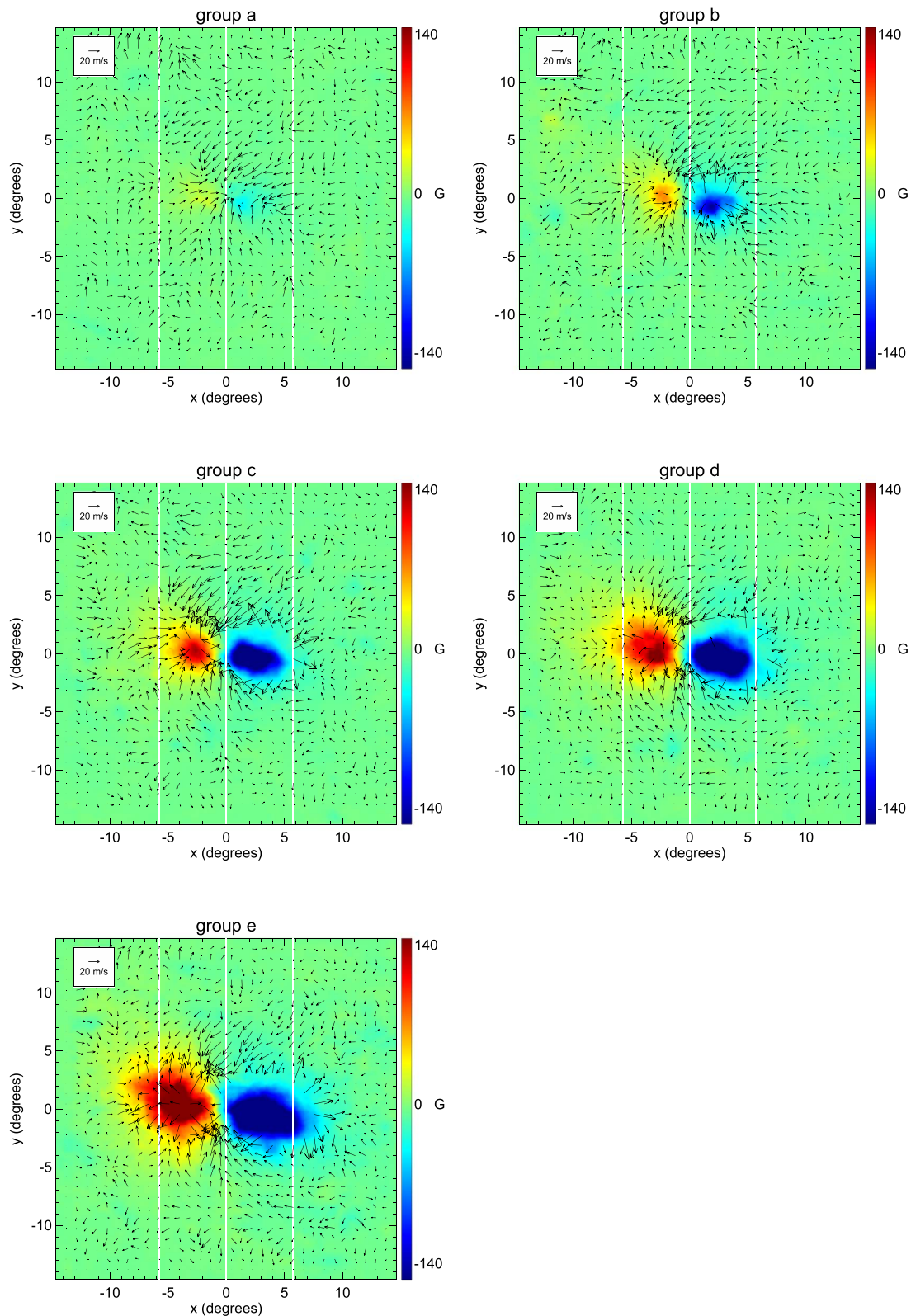


**Figure 6.** Ensemble-averaged flows for each of the five flux groups as indicated. The background shows the ensemble-averaged signed magnetic-flux density. As discussed in the text, a latitude-dependent smoothly varying flow was assessed and subtracted from the flows shown here. Converging flows are prominent above and below the ARs. Outflows from sunspots are suppressed in the larger flux groups (groups (c), (d), and (e)) for clarity. Vertical white lines isolate the leading (right) and trailing (left) regions of the active regions for further analysis (see the text).

indicate amplitudes on the order of a few  $\text{m s}^{-1}$  (e.g., Howe 2009; Gizon et al. 2010) and, for the most part, are spatially correlated with latitudes of solar activity. AR inflows and,

likely the retrograde flows that accompany them, have sufficient magnitude to contribute to these global measurements. For example, just three ARs on the Sun at sufficiently

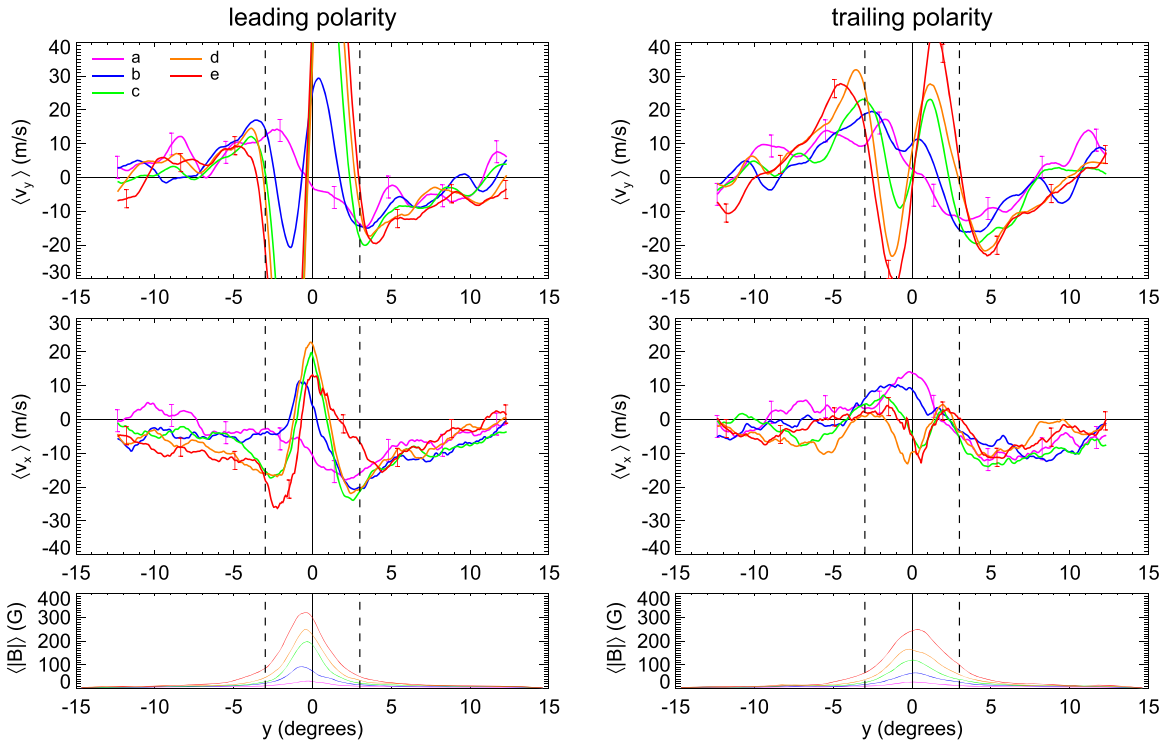


**Figure 7.** Averages over longitude of the group-averaged flow components, and magnetic flux density, across the leading and trailing polarity zones. The panels on the left (right) show the results for the leading (trailing) zones, with the top (middle) panels showing the averages of  $v_y$  ( $v_x$ ) respectively. Each group is denoted by a different line color as indicated in the figure legend. Only a few  $1\sigma$  error bars (denoting the error of the mean over the group) are shown to avoid clutter and are typical of all of the errors. Averages of the unsigned magnetic flux density over each of the polarity zones are shown in the bottom panels, with the same colors as the flow averages. The vertical dashed lines bound the region within  $\pm 3^\circ$  of the AR center to guide the relevant discussion in the text.

close latitudes would contribute about a  $1 \text{ m s}^{-1}$  signal to a longitudinal average of either the meridional or zonal flow, assuming each AR is characterized with a  $10 \text{ m s}^{-1}$  flow spanning about  $12^\circ$  (the combined range of both polarity regions as defined in this work). The ensemble averages presented above demonstrate that even weak ARs (with fluxes on the order of a few  $10^{21} \text{ Mx}$ ) could contribute detectable amounts to these global flows.

The large reduction of (largely supergranulation-dominated) noise in our averaged AR flow maps makes feasible the use of these maps in making improved predictions on AR contributions to global flows. We present a simple proof-of-concept of this, while leaving a more detailed analysis to future work. This demonstration makes use of the synoptic maps for Carrington rotations 2099 and 2149 near solar minimum and maximum respectively (Figure 1 shows the magnetogram for CR 2149). For each rotation, we identify the flux group of all of the ARs included in our survey and remap the appropriate group-averaged flow components back to Carrington coordinates. Longitudinal averages are then performed, with the results shown in Figure 8. Smoothing (over a width of  $6^\circ$  in latitude) is applied to the curves shown in this plot, in order to simulate a more realistic assessment (which, for example, might involve averages over multiple rotation periods). The use of nearby quiet-Sun regions to fit and remove background trends (Section 3.1) implies that the net contributions shown in Figure 8 represent hypothetical perturbations to the mean (quiet-Sun) meridional and zonal flow components.

The predicted contributions ( $\delta v_L$ ,  $\delta v_B$ ) to the zonal and meridional flows, respectively, are shown in Figure 8. They are both on the order of several  $\text{m s}^{-1}$ , which confirms that the AR

flows characterized in this survey are plausibly detectable in global averages. It is noteworthy that, for the meridional component, the perturbations to the mean meridional circulation take the form of converging zones centered (at least approximately) on the mean latitudes of activity, which is qualitatively consistent with the observed modulation of meridional circulation observed near solar maximum (Chou & Dai 2001; Gizon 2003; Zhao & Kosovichev 2004; Zhao et al. 2014).

The results for the zonal components show predicted perturbations of similar magnitude to the meridional components, but having a notably different variation with latitude. In particular, the contributions are predominantly of one sign (corresponding to a net retrograde motion) and have peaks displaced significantly in latitude toward the poles relative to the mean AR latitudes. This offset is apparently attributable to the polar/equatorward amplitude asymmetry in the retrograde flows noted earlier. For both rotations, these retrograde flows appear to dominate or at least cancel out, the more spatially compact prograde motions observed in (primarily) the strongest ARs. We note the consistency of the residual retrograde flows observed in Figure 8 with the general pattern of the torsional oscillation, whereby ARs tend to center on the boundaries between faster (in the polar direction) and slower (in the equatorial direction) flow bands. Further interpretations of the results shown here need to be tempered by the intimidating number of details specific to how the zonal flow residuals, as well as the meridional flow, are obtained. Nevertheless, it seems unavoidable that AR flows provide a detectable contribution to global flow measurements.

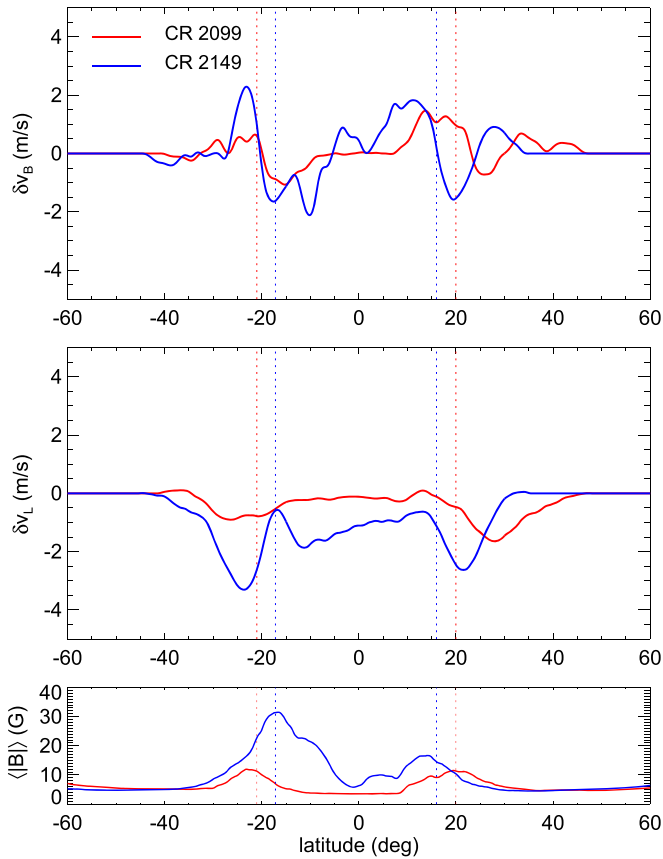


**Figure 8.** Hypothetical contributions to large-scale, longitude averaged, meridional (top panel) and zonal (middle panel) flows from active regions sampled in the synoptic maps of Carrington rotations 2099 and 2149 (i.e., close to solar minimum and maxima of cycle 24 respectively). A box-car smoothing with a width of  $6^\circ$  in latitude has been applied to the curves shown here. The bottom panel shows the longitudinal average of the line-of-sight magnetic flux density from HMI synoptic magnetograms. Vertical dotted lines in all panels indicate the centroid positions of the magnetic flux density as shown in the bottom panel.

#### 4. Discussion and Conclusions

We have measured and compared AR flows, as determined using HH, and averaged over samples of about 1000 measurements within each of five groups of magnetic flux. Principle results include the detection of both converging and retrograde motions extending out to  $\sim 10^\circ$  in latitude beyond the AR centers. Differences between flows associated with the leading and trailing polarities, and among the difference flux groups are noted in Section 3.3.

Our measurements of the converging flows demonstrate the consistency of their general properties across a range of flux exceeding an order of magnitude. These inflows are similar to those inferred from ensemble averages made with local-correlation tracking methods (Löptien et al. 2017), including a preferential inflow to the trailing polarity. Our study uses a larger set of AR flow measurements, and includes ARs with weaker flux, than Löptien et al. (2017). The converging flows we observe are also consistent with the inflow values of  $20\text{--}30\text{ m s}^{-1}$  which Hindman et al. (2009) found flowing into the “periphery” of ARs, as defined by a 50 G contour in MDI magnetograms after smearing to a  $2^\circ$  resolution.

Our ensemble averages show the presence of retrograde flows that straddle (primarily) the polar and (to a lesser degree) equatorial sides of ARs across the entire flux range studied.

These appear to be heretofore unknown or, at least, unresolved in prior studies. However, the predominance of  $10\text{ m s}^{-1}$  retrograde flows flanking the polar side of ARs is plausibly consistent with the net cyclonic circulation of  $\sim 5\text{ m s}^{-1}$  found by Hindman et al. (2009) around AR peripheries. On the other hand, the retrograde flows do not readily appear in the ensemble-averaged flow map shown in Figure 8 of Löptien et al. (2017). This discrepancy is not understood, but may result from differences in the background trend removal or other details in the analyses. Applying both HH and local-correlation-tracking methods to identical AR samples would be highly useful in exploring and understanding these differences.

Based on the estimates presented in Section 3.4, the degree to which the retrograde flows may contribute to published measurements of the torsional oscillation is a fair question. It is worth emphasizing that the ensemble-averaged flows shown in Figure 6 represent residuals after the subtraction of a latitude-dependent background contribution assessed from quiet regions straddling the ARs. This procedure removes any real latitude-dependent zonal flow component that is invariant with longitude but departs from the tracked Carrington rotation rate. Therefore, the retrograde flows presented here are spatially associated with the ARs, represent a departure from the zonal flow present in the nearby quiet regions, and do not, for example, result from the choice of tracking rate. Further studies, similar to those carried out by González Hernández et al. (2008) and designed to isolate and compare flow contributions between quiet regions and ARs, are critical to fully understanding the relation of the AR-specific flows presented here with longitudinal averaged global flows.

It would be useful to improve and expand the analysis presented here in order to study the dependence of flows with other active-region properties, or to examine their temporal variation as ARs evolve. Extending the analysis to regions with fluxes below  $10^{21}\text{ Mx}$  is also of interest. Determining and validating the depth variation of the flows, particularly using helioseismic methods with high spatial resolution, remain an important area for study. Inferring subsurface flows from travel-time measurements potentially compromised by the presence of strong magnetic fields remains a critical problem in local helioseismology.

Martin Woodard provided valuable comments on a draft of this work. We are grateful to Charles Baldner and the rest of the Helioseismic and Magnetic Imager (HMI) team at Stanford University for computing and providing the custom data sets for this study. This work is supported by the Solar Terrestrial program of the National Science Foundation (grant AGS-1623844) and by the NASA Heliophysics Division through its Heliophysics Supporting Research (grant 80NSSC18K0066) and Guest Investigator (grant 80NSSC18K0068) programs. Resources supporting this work were provided by the NASA High-End Computing (HEC) Program through the NASA Advanced Supercomputing (NAS) Division at Ames Research Center. *SDO* data is provided courtesy of NASA/*SDO* and the AIA, EVE, and HMI science teams.

#### Appendix A

##### Validation of Calibrated Flows Using MHD Simulations

Validating methods used to infer flows, particularly in the presence of strong magnetic fields typical of ARs, is critical to

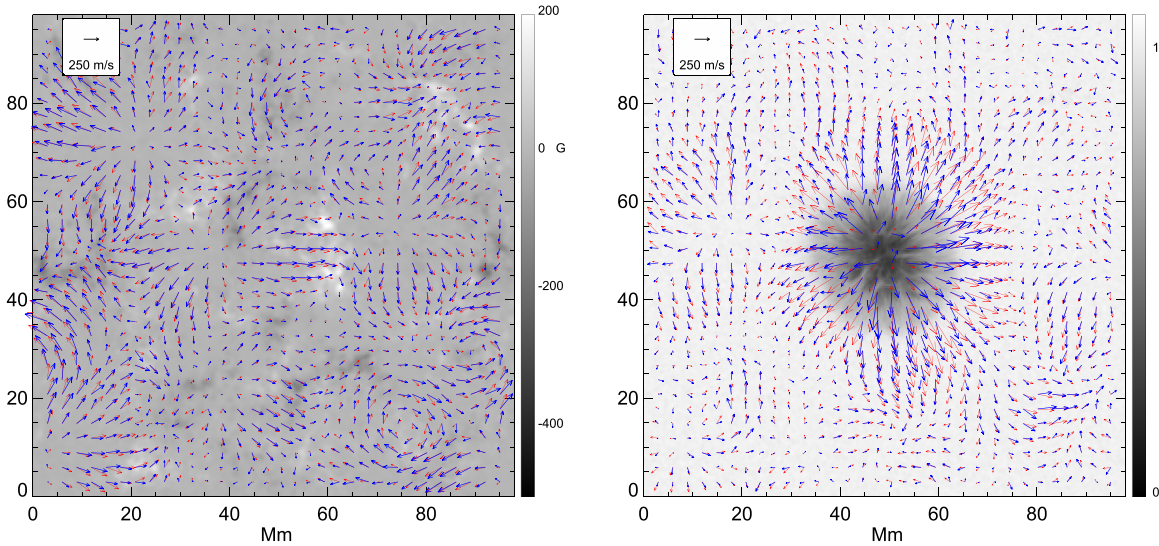


**Figure 9.** Comparisons of true flows (red arrows) with calibrated-HH flows (blue arrows) using artificial data extracted from two numerical simulations (see the text). The left panel shows the results for a quiet-Sun convective simulation, with the background indicating the time average of the vertical magnetic flux density. Temporal averaging and spatial smearing of the true flows are performed as described in the text. The flows are comparable to those present in solar supergranulation in both size and magnitude. A correlation coefficient of 0.92 is found between the individual flow components ( $v_x$ ,  $v_y$ ) of the true and inferred flows. The right panel shows the results for the sunspot simulation, with the background showing a snapshot of photospheric intensity normalized to the quiet photosphere. While there is qualitative agreement between the true and inferred moat flows (with a correlation coefficient of 0.85), the inferred outflows inside (outside) the penumbra appear overestimated (underestimated) compared to the actual flows.

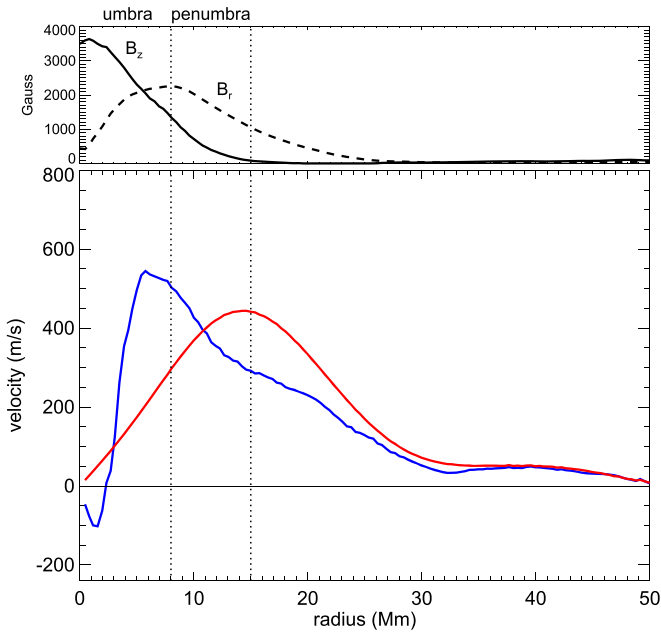


**Figure 10.** Top panel shows azimuthal averages of the vertical ( $B_z$ ) and radial ( $B_r$ ) component of the photospheric magnetic flux density from a time-average of the sunspot simulation. The bottom panel shows azimuthal averages of radial flow components. The radial component (of either the flux density or flow) is defined as the projection of the horizontal component along a radius extending from the center of the sunspot. The red curve shows the result for the true flows (after time-averaging and spatially smearing). The blue curve shows the result for the calibrated-HH flows. Discrepancies between the two are most obvious within the spot but also extend notably beyond the penumbra.

correctly interpreting the results. Uncertainties and discrepancies in helioseismic inferences about sunspots are well known (e.g., Gizon et al. 2009; Moradi et al. 2010; Braun et al. 2012). Effects that contribute to these uncertainties include, but are not limited to (1) the likely presence of strong near-surface

magnetic and thermal perturbations in sunspots that are inconsistent with the Born approximation or other enabling assumptions (e.g., Braun & Birch 2006; Couvidat & Rajaguru 2007; Crouch et al. 2011; Braun et al. 2012), (2) wave phenomena including absorption and mode conversion (e.g., Woodard 1997; Crouch et al. 2005; Schunker et al. 2008), (3) consequences of magnetically suppressed p-mode amplitudes (Rajaguru et al. 2006), and (4) the distortion of the spectral line used to assess Doppler shifts in strong fields as well as instrumental and calibration limitations (e.g., Wachter et al. 2006; Rajaguru et al. 2007). Some of these phenomena have been investigated in the context of thermal structure modeling but less is known about their potential influence on flow measurements.

Agreement between flows inferred from different helioseismic methods (Hindman et al. 2004), and between helioseismic and nonhelioseismic methods (Liu et al. 2013; Birch et al. 2016; Jain et al. 2016), provide some confidence in the procedures and the results obtained. On the other hand, these comparisons are potentially compromised by the lack of knowledge of the actual flow fields present. This problem is resolved by the use of artificial data, such as provided in realistic magnetohydrodynamic (MHD) simulations. Here, we use two publicly available<sup>1</sup> target simulations. The first of these is of quiet-Sun convection in the presence of a small-scale dynamo (Rempel 2014) which has been used to validate forward and inverse methods in both time-distance helioseismology (DeGrave et al. 2014b) and HH (DeGrave et al. 2018). The simulation covers a  $98.304 \times 98.304 \times 18.432$  Mm domain, computed with  $64 \times 64 \times 32$  km resolution, a total duration of 30 hr, and a time step of 0.9 s. As in DeGrave et al. (2018), we employ the first 15 hr of artificial Dopplergrams from this run. The second simulation is a sunspot with a magnetic flux of approximately  $6 \times 10^{21}$  Mx and contained in an identical domain, but computed at a  $48 \times 48 \times 24$  km

<sup>1</sup> [http://download.hao.ucar.edu/pub/rempel/sunspot\\_models](http://download.hao.ucar.edu/pub/rempel/sunspot_models)

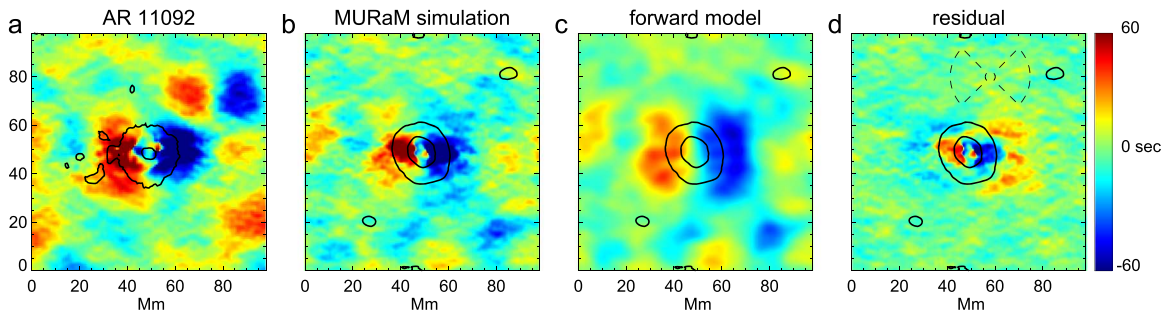


**Figure 11.** Comparison of west-minus-east (WE) travel-time differences. Panel (a) shows the WE travel-time difference for one the sunspot regions used in this study (AR 11092). The area is cropped to the same dimension of the WE travel-time difference measured in the sunspot simulation of Rempel (2015), which is shown in panel (b). Panel (c) shows the predicted travel-time difference (or “forward model”) obtained by a convolution the sensitivity function with a time-average of the three-dimensional flows present in the simulation. Panel (d) shows the residual signal after subtracting the forward model from the measurement. Black contours indicate time-averaged vertical magnetic flux density values of 300 and 2000 G. In panel (d) the dashed lines show the geometry of the east and west pupils used in the measurement.

resolution and a time step of 0.45 s. The simulation shows a sunspot with a penumbra and Evershed flow (Rempel 2015). This run was carried out for 100 hr, of which we use a 15 hr interval starting 57.5 hr into the run, by which time a realistic moat flow has developed.

The background atmosphere in both simulations has a vertical stratification consistent with Model S, for which we apply lateral-vantage holography with unmodified Greens functions (see, for example, DeGrave et al. 2018) at a focus depth of 3 Mm. For comparison with the measured calibrated flows, we use time-averages of the true flows present in the simulation as sampled at fixed intervals (which are 83.3 and 30 minutes for the quiet-Sun convective and sunspot simulations respectively). Consistent with the working assumptions for the calibrated-HH method (Section 2.3), we extract only the horizontal flow components and apply a horizontal smoothing with a two-dimensional Gaussian function with an FWHM of 14 Mm in the direction along the component axis, and 9 Mm in the perpendicular direction. This smearing is comparable to the horizontal extent of the appropriate sensitivity functions as illustrated by Braun et al. (2007) and DeGrave et al. (2018) and thus removes small-scale noise. The true flows are also averaged in depth with a weighting given by the function shown in Figure 4. Figure 9 shows comparisons of the calibrated flows with the temporally averaged and spatially smeared true flows for both simulations.

The results show good agreement in the quiet-Sun convective case, as well as at least qualitative agreement for the sunspot flows. For the quiet and sunspot simulations we find a correlation coefficient of 0.92 and 0.85, respectively, between the individual flow components ( $v_x$ ,  $v_y$ ) of the true and inferred flows. However, a closer examination shows that the inferred Evershed flows (within the penumbra) using the calibrated-HH method appear to be overestimated while most of the moat flows (extending beyond the penumbra) are underestimated. This is best seen in Figure 10, which shows the azimuthal averages of the radial flow component (with respect to the sunspot center).

To explore these discrepancies further, we employ the sensitivity functions derived in prior work (DeGrave et al. 2018)

to examine differences between the actual travel-time difference measurements with those predicted under the assumption of the Born approximation. Such a comparison removes potential issues arising from the assumptions specific to the calibrated-HH method. A detailed study of the quiet-Sun simulation, in the context of the forward-modeling problem, was already performed by DeGrave et al. (2018). They found that a comparison of all lateral-vantage HH measurements (including the focus depth of 3 Mm employed here) with the forward prediction from the sensitivity functions showed excellent agreement within the realization noise. A comparison of results for the sunspot simulation, however, gives a notably different picture (e.g., Figure 11). Specifically, the measured travel-time differences show the presence of an artifact that is revealed after the predicted model travel-time differences are subtracted from the measurements. This artifact takes the form of a spurious outflow within the penumbra in addition to another spurious inflow extending about 15 Mm beyond the penumbra. The cause of this artifact is unknown, but apparently it represents a failure of the sensitivity function to fully account for the physics of wave propagation in the presence of strong magnetic flux (examples of relevant issues are listed in Appendix A). We note that this artifact has implications beyond the use of the calibrated-HH method and will presumably adversely affect any inverse or forward modeling based on standard (Born approximation-based) methodology. Comparisons using different lateral-vantage HH measurements confirm that the spatial extent of the artifacts are apparently related to the geometry of the pupils used. Notably, the maximum amplitude of the artifacts appear in locations where either the umbra or penumbra fill one of the pupil quadrants.

## Appendix B Ensemble Averages Including Sunspot Flows

Figure 12 shows a version of Figure 6 without the suppression of the strong (mostly diverging) flows observed in the centers of the ARs. These diverging flows arise from the contribution of moat flows around sunspots in each flux group.

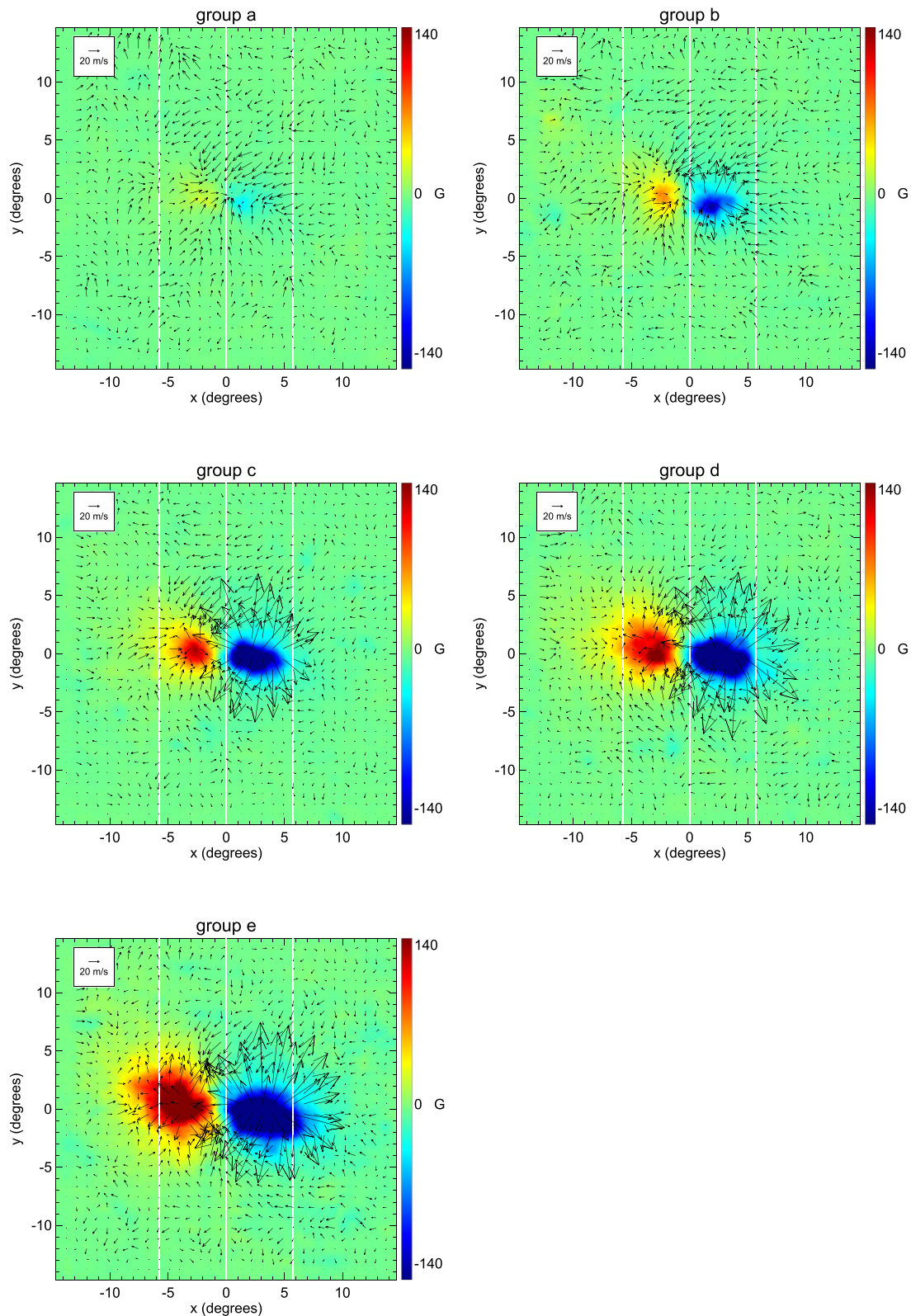


**Figure 12.** Ensemble-averaged flow fields for each flux group, as in Figure 6, but without the suppression of the strong, mostly diverging, flows due to the contribution of sunspot moats in the averaging.

### Appendix C Magnetic Masking Test

Given the results of our validation studies with numerical simulations (Appendix A) we investigate how our flow

measurements may be compromised by artifacts caused by regions of magnetic flux typical of sunspots. To assess the degree of potential contamination of our results, we perform ensemble averages of the flow components as in Section 3.2

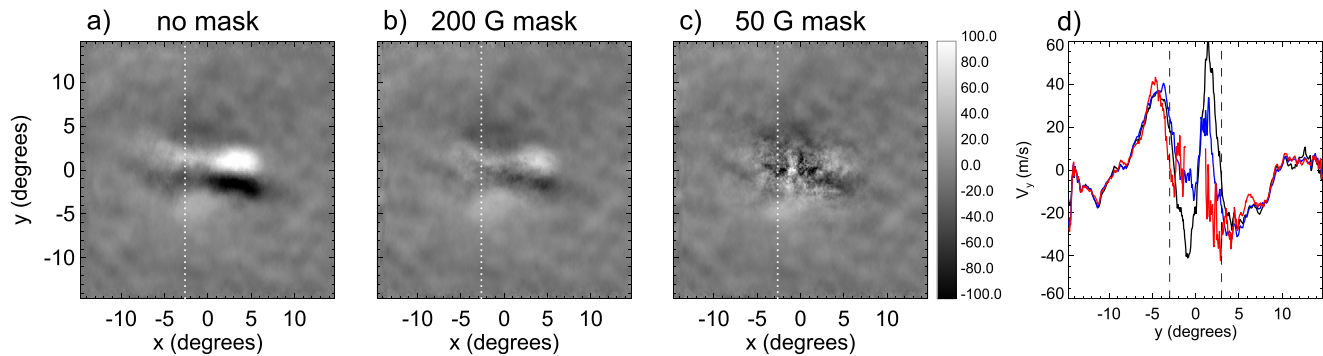


**Figure 13.** Results from masking tests designed to reveal the dependence on (and possible contamination from) the inclusion of strong magnetic regions in the ensemble averaging. Panel (a) shows the poleward flow component  $v_y$ , averaged over the ARs in group (e), and after detrending (Section 3.1). Panel (b) shows the same average, but after masking out flows within pixels of the individual flow maps with flux density greater than 200 G. Panel (c) shows the average using a magnetic threshold of 50 G. Panel (d) shows a comparison of vertical cuts along the dotted lines shown in panels (a)–(c). The black curve indicates the results for the unmasked flows, while the blue (red) curve shows the results using the 200 (50) G masks. The vertical dashed lines bound the region within  $\pm 3^\circ$  of the AR center. Within the AR center the strong flow signatures are reduced using the 200 G mask and become noisy with the 50 G mask. A portion of the 50 G measurements in panel (d) close to the AR is omitted to avoid obscuring the plot with noise. The main result of this test is that the more extended converging signatures remain robust with respect to the masking.

but set the flows in the individual maps to zero in regions above a given magnetic flux density. This data masking is not meant as a “correction,” but is rather a test of where and how much results change between the masked and unmasked averaging. Control tests with magnetic masks are commonly used in helioseismology (e.g., Zhao & Kosovichev 2003; Korzennik 2006; González Hernández et al. 2008; Liang & Chou 2015). Figure 13 shows the results for the strongest flux group, representing the worst-case scenario, and using masks with threshold flux densities of 200 and 50 G. The masks are constructed using a potential-field extrapolation of the total field from the line-of-sight (time-interval averaged) magnetograms as described by Braun (2016). Examples of the masks as applied to an AR are shown in Figure 1 of Braun (2016). The 200 G mask removes flows within sunspot umbra and penumbra that are identified as the most problematic regions in Appendix A. The 50 G mask removes weaker fields around the ARs and provides even stronger constraints on potential contamination. Results show little change in inferences of  $v_y$  between masked and unmasked averaging for distances beyond about  $3^\circ$  from the AR center. Within  $3^\circ$  the flow signals are reduced using the 200 G threshold, apparently due to the exclusion of Evershed and other sunspot flows from the average. For the 50 G threshold, the averaged flows within the AR become dominated by noise. This is likely due to poorer statistics (i.e., fewer nonzero pixels) in the averaging. The results, however, appear to establish a relatively high confidence in the more extended inflows and retrograde motions, which was the primary purpose of this test.

### ORCID iDs

D. C. Braun  <https://orcid.org/0000-0001-6840-2717>

### References

- Birch, A. C., Schunker, H., Braun, D. C., et al. 2016, *SciA*, **2**, e1600557  
 Braun, D. C. 2016, *ApJ*, **819**, 106  
 Braun, D. C., & Birch, A. C. 2006, *ApJL*, **647**, L187  
 Braun, D. C., Birch, A. C., Benson, D., Stein, R. F., & Nordlund, A. 2007, *ApJ*, **669**, 1395  
 Braun, D. C., Birch, A. C., & Lindsey, C. 2004, in ESA Special Publication 559, SOHO 14 Helio- and Asteroseismology: Towards a Golden Future, ed. D. Danesy (Noordwijk: ESA), 337  
 Braun, D. C., Birch, A. C., Rempel, M., & Duvall, T. L., Jr. 2012, *ApJ*, **744**, 77  
 Braun, D. C., & Wan, K. 2011, *JPhCS*, **271**, 012007  
 Cameron, R. H., & Schüssler, M. 2012, *A&A*, **548**, A57  
 Chou, D.-Y., & Dai, D.-C. 2001, *ApJL*, **559**, L175  
 Couvidat, S., & Rajaguru, S. P. 2007, *ApJ*, **661**, 558  
 Crouch, A. D., Birch, A. C., Braun, D. C., & Clack, C. T. M. 2011, in IAU Symp. 273, The Physics of Sun and Star Spots, ed. D. P. Choudhary & K. G. Strassmeier (Cambridge: Cambridge Univ. Press), 384  
 Crouch, A. D., Cally, P. S., Charbonneau, P., Braun, D. C., & Desjardins, M. 2005, *MNRAS*, **363**, 1188  
 DeGrave, K., Braun, D. C., Birch, A. C., Crouch, A. D., & Javornik, B. 2018, *ApJ*, **863**, 34  
 DeGrave, K., Jackiewicz, J., & Rempel, M. 2014a, *ApJ*, **794**, 18  
 DeGrave, K., Jackiewicz, J., & Rempel, M. 2014b, *ApJ*, **788**, 127  
 Gizon, L. 2003, PhD thesis, Stanford Univ.  
 Gizon, L., Birch, A. C., & Spruit, H. C. 2010, *ARA&A*, **48**, 289  
 Gizon, L., Duvall, T. L., Jr., & Larsen, R. M. 2001, in IAU Symp. 203, Recent Insights into the Physics of the Sun and Heliosphere: Highlights from SOHO and Other Space Missions, ed. P. Brekke, B. Fleck, & J. B. Gurman (San Francisco, CA: ASP), 189  
 Gizon, L., Duvall, T. L., Jr., & Schou, J. 2003, *Natur*, **421**, 43  
 Gizon, L., Schunker, H., Baldner, C. S., et al. 2009, *SSRv*, **144**, 249  
 González Hernández, I., Kholikov, S., Hill, F., Howe, R., & Komm, R. 2008, *SoPh*, **252**, 235  
 Haber, D. A., Hindman, B. W., Toomre, J., & Thompson, M. J. 2004, *SoPh*, **220**, 371  
 Hindman, B. W., Gizon, L., Duvall, T. L., Jr., Haber, D. A., & Toomre, J. 2004, *ApJ*, **613**, 1253  
 Hindman, B. W., Haber, D. A., & Toomre, J. 2009, *ApJ*, **698**, 1749  
 Howe, R. 2009, *LRSF*, **6**, 1  
 Jain, K., Tripathy, S. C., Ravindra, B., Komm, R., & Hill, F. 2016, *ApJ*, **816**, 5  
 Jiang, J., Hathaway, D. H., Cameron, R. H., et al. 2014, *SSRv*, **186**, 491  
 Jiang, J., Işık, E., Cameron, R. H., Schmitt, D., & Schüssler, M. 2010, *ApJ*, **717**, 597  
 Komm, R., & Gosain, S. 2015, *ApJ*, **798**, 20  
 Komm, R., Howe, R., Hill, F., et al. 2007, *ApJ*, **667**, 571  
 Komm, R., Howe, R., & Hill, F. 2011, *SoPh*, **268**, 407  
 Korzennik, S. G. 2006, in Proc. SOHO 18/GONG 2006/HELAS I, Beyond the Spherical Sun, ed. K. Fletcher & M. Thompson (ESA SP-624; Noordwijk: ESA), 60  
 Liang, Z.-C., & Chou, D.-Y. 2015, *ApJ*, **805**, 165  
 Lindsey, C., & Braun, D. C. 2004, *ApJS*, **155**, 209  
 Liu, Y., Zhao, J., & Schuck, P. W. 2013, *SoPh*, **287**, 279  
 Löptien, B., Birch, A. C., Duvall, T. L., et al. 2017, *A&A*, **606**, A28  
 Martín-Belda, D., & Cameron, R. H. 2017, *A&A*, **597**, A21  
 Moradi, H., Baldner, C., Birch, A. C., et al. 2010, *SoPh*, **267**, 1  
 Rajaguru, S. P., Birch, A. C., Duvall, T. L., Jr., Thompson, M. J., & Zhao, J. 2006, *ApJ*, **646**, 543  
 Rajaguru, S. P., Sankarasubramanian, K., Wachter, R., & Scherrer, P. H. 2007, *ApJL*, **654**, L175  
 Rempel, M. 2014, *ApJ*, **789**, 132

- Rempel, M. 2015, [ApJ](#), 814, 125
- Rincon, F., & Rieutord, M. 2018, [LRSP](#), 15, 6
- Schunker, H., Braun, D. C., Lindsey, C., & Cally, P. S. 2008, [SoPh](#), 251, 341
- Upton, L., & Hathaway, D. H. 2014, [ApJ](#), 792, 142
- Wachter, R., Schou, J., & Sankarasubramanian, K. 2006, [ApJ](#), 648, 1256
- Wang, Y.-M., Sheeley, N. R., Jr., & Lean, J. 2002, [ApJ](#), 580, 1188
- Woodard, M. F. 1997, [ApJ](#), 485, 890
- Zhao, J., Georgobiani, D., Kosovichev, A. G., et al. 2007, [ApJ](#), 659, 848
- Zhao, J., & Kosovichev, A. G. 2003, [ApJ](#), 591, 446
- Zhao, J., & Kosovichev, A. G. 2004, [ApJ](#), 603, 776
- Zhao, J., Kosovichev, A. G., & Bogart, R. S. 2014, [ApJL](#), 789, L7